This is the peer-reviewed, final accepted version for American Mineralogist, published by the Mineralogical Society of America.
The published version is subject to change. Cite as Authors (Year) Title. American Mineralogist, in press.
DOI: https://doi.org/10.2138/am-2022-8843. http://www.minsocam.org/

Word Count: 10357

Cathodoluminescence of iron oxides and oxyhydroxides

Nir Galili[§,*], Ifat Kaplan-Ashiri[†] and Itay Halevy[§]

[§]Department of Earth and Planetary Sciences, Weizmann Institute of Science, Rehovot 76100, Israel.

[†]Department of Chemical Research Support, Weizmann Institute of Science, Rehovot 76100, Israel.

[*]Correspondence: ngalili@ethz.ch

Manuscript information:

Nir Galili, ngalili@ethz.ch, current address: Geological Institute, Department of Earth Sciences, ETH Zürich, Zürich 8092, Switzerland.

Ifat Kaplan-Ashiri, ifat.kaplan-ashiri@weizmann.ac.il

Itay Halevy, itay.halevy@weizmann.ac.il

Abstract

Iron oxides and oxyhydroxides show promise as superconductor materials and as repositories of paleoenvironmental information. However, there are no microscale nondestructive analytical techniques to characterize their combined mineralogy, chemical composition, and crystal properties. We address this by developing cathodoluminescence mounted on a scanning electron microscope (SEM-CL) as an in situ nondestructive method for crystallographic and petrographic study of iron oxides and oxyhydroxides. We show that goethite, hematite, and magnetite display

This is the peer-reviewed, final accepted version for American Mineralogist, published by the Mineralogical Society of America.
The published version is subject to change. Cite as Authors (Year) Title. American Mineralogist, in press.
DOI: https://doi.org/10.2138/am-2022-8843. http://www.minsocam.org/

different SEM-CL spectra, which may be used for mineral identification. We further show that different formation pH, manganese substitution for iron in goethite and hematite, and titanium substitution for iron in magnetite, cause shifts in the SEM-CL spectra of these minerals. These spectral shifts are not always detectable as a change in the emission color but are easily discernable by quantitative analysis of the spectra. Together with subtle but observable variations in the SEM-CL spectra of natural goethite and hematite, we suggest that these dependences of the SEM-CL spectra on pH and chemical composition may be used as a means of identifying multiple episodes of mineralization and recrystallization. We apply the newly developed SEM-CL methods to two polished sections of natural samples and show that quantitative analysis of the spectra obtained allows identification of differences between varieties of the same mineral that are not observable by other means. Like the application of SEM-CL to geologic samples in this study, we suggest that this approach may be used to explore the in situ chemistry and crystallinity of a variety of natural and manufactured iron oxides and oxyhydroxides.

Keywords: Scanning electron microscope, petrography, mineralogy, non-destructive spectroscopy

Introduction

Applications of cathodoluminescence (CL) imaging in geoscience and materials science harness the characteristic emission of visible light from crystalline materials bombarded by high-energy electrons to study the internal structure and composition of natural and engineered materials. Examples include determination of trace element concentrations in minerals, mapping of defects in semiconductors, and constraining the (re)crystallization history of rocks (Boggs and Krinsley, 2006). Variation in the CL spectrum, typically described in terms of changes in the color of emitted light, arise from impurities or defects, and may be related to variations in the material's

formation conditions (e.g., parent fluid chemical composition, temperature, rate). Consequently, in the geosciences, CL has been used to study the formation and alteration of minerals of various origins (Barker et al., 1991; Tarashchan and Waychunas, 1995; Boggs and Krinsley, 2006).

Goethite (α-FeOOH), hematite (α-Fe_2O_3) and magnetite (Fe_3O_4) are the three most common naturally-occurring Fe oxides and oxyhydroxides (Cornell and Schwertmann, 2003). They occur in a variety of marine sediments and sedimentary rocks, some of which are major economic sources of Fe, as well as in soils, bog deposits and spring deposits (Schwertmann and Cornell, 1991; Yapp, 2001). In addition to their economic significance, the widespread occurrence and geologic abundance of Fe oxides and oxyhydroxides suggests their potential as repositories of information about various environmental and Earth-history properties. Indeed, Fe oxides have been used to study the geologic history of seawater oxygen isotopes (Galili et al., 2019), the evolution of atmospheric oxygen concentrations (Holland, 1984 and references therein), past ocean redox conditions (Sperling et al., 2015; Stolper and Keller, 2018), the genesis and subsequent alteration of banded iron formations (Ahn and Buseck, 1990; Bekker et al., 2010; Rasmussen et al., 2016; Konhauser et al., 2017), and past (micro)biological Fe-related metabolic activity (Heimann et al., 2010; Craddock and Dauphas, 2011). For all such applications, it is necessary to assess the fidelity of the Fe oxides and oxyhydroxides as repositories of paleo-environmental information, and this is hindered by the difficulty in applying petrographic methods to study these minerals. For example, all Fe oxides and oxyhydroxides are opaque in transmitted light microscopy, but bright in scanning-electron microscopic imaging (Goldstein et al., 2017). Reflected light microscopy techniques have been used in the past to study Fe oxides, both visually (e.g., Howie et al., 1992) and by inspection of reflectance at specific wavelengths (e.g., Pirard and Lebichot, 2004). However, limited lateral resolution, a relatively low detection

limit, and color and wavelength band overlaps between different Fe oxides (e.g., lepidocrocite and goethite; Scheinost et al, 1998) limit the utility of such approaches and motivate the development of alternative methods, such as CL.

Traditionally, CL imaging has been used in the analysis of silicate, phosphate, and carbonate minerals, while for other minerals, among which are Fe oxides and oxyhydroxides, the method has been considered inapplicable due to much poorer self-luminescence (Frimmel, 1997; Šťastná and Přikryl, 2009; Črne et al., 2014). Moreover, even low concentrations of Fe are documented to effectively quench CL emission of otherwise highly luminescent minerals (Barker et al., 1991; Tarashchan and Waychunas, 1995). The low CL of Fe oxides and oxyhydroxides is thought to originate from weak ligand field splitting for complexes of transition metals in the fourth row of the periodic table, which results in a rapid deactivation of charge-transfer states (Šima, 2015).

The study of low-luminescence minerals, including Fe oxides and oxyhydroxides, faces two main challenges. Firstly, emission from high-luminescence minerals (e.g., quartz and carbonate minerals) obscures the emission from the weakly luminescent minerals of interest. Secondly, very few reference CL spectra of the low-luminescence minerals are available for interpretation of measured spectra of natural and synthetic materials. In part, these two challenges are related to the historic use of CL systems mounted on optical microscopes (OM-CL), which lack the range of magnifications, the spatial resolution and sensitivity of newer, scanning electron microscope-based instruments (SEM-CL). In SEM-CL instruments, detection of spatially small, weakly luminescent features is possible, and interference from high-luminescence minerals is low due to a smaller interaction volume between the electron beam and the sample (Goldstein et al., 2017).

Given the prominence and utility of Fe oxides and oxyhydroxides in natural environments and the rock record, as well as their inaccessibility to petrographic approaches, we here developed

SEM-CL as a means of overcoming obstacles to the application of CL to these minerals. We analyzed both synthetic (laboratory-precipitated) and geologic samples and decomposed their spectra to quantify variations that do not manifest as emission color changes discernable by eye. By integrating multiple analytical methods, we verified that different Fe oxide and oxyhydroxide minerals have unique CL spectra, which can be used as a nondestructive, in situ mineral identification tool. In addition, by studying a series of laboratory-precipitated Mn-substituted hematite and goethite, we here show that metal impurities in the lattice of Fe oxide and oxyhydroxide minerals modify the minerals' CL spectra. This, in addition to other possible effects of the mineral formation conditions on CL spectra, suggests the utility of SEM-CL as a tool to distinguish Fe oxides and oxyhydroxides formed under different environmental and chemical conditions (i.e., to detect different generations of a mineral) within a single geologic sample. We demonstrate this utility by applying the developed methods to two natural rock samples.

Materials and Methods

The methodology was developed to achieve three objectives. The first was the production of a set of monomineralic reference materials with a well-constrained formation environment, which would be systematically analyzed and included in a new SEM-CL database of Fe oxides and oxyhydroxides. We accomplished this by synthesizing Fe oxides and oxyhydroxides in the laboratory, by several different techniques, and analyzing the samples by various methods, as described below. The second objective was to constrain the effect of metal substitution for Fe on the SEM-CL emission spectrum of Fe oxides and oxyhydroxides. For this purpose, we produced a set of Mn-substituted goethite and hematite, which were synthesized with increasing substitution of Mn for Fe in the crystal lattice. The third objective was to test the methods

developed here on natural samples containing Fe oxides and oxyhydroxides within their original matrix of both high- and low-luminescence minerals. For this purpose, we produced and analyzed a polished section of two rock samples, as described below.

Information from several analytical methods was combined to provide an understanding of the studied materials and relate their properties to their SEM-CL spectra. X-ray powder diffraction (XRD) was used to determine the mineralogy and constrain the effects of Mn substitution for Fe on mineral lattice parameters. Fourier transform infrared (FTIR) spectroscopy was used for mineral identification and to provide information on the molecular structure of the Mn-substituted goethite and hematite. Inductively coupled plasma mass spectrometry (ICP-MS) was used to measure the amount of Mn incorporated into the Mn-substituted goethite and hematite lattice, and to determine the elemental composition of the various Fe oxides and oxyhydroxides studied. Raman microscopy was used for in situ mineral identification as a means of validating the SEM-CL results. Lastly, energy-dispersive X-ray spectroscopy on a scanning electron microscope (SEM-EDS) was used to examine the elemental composition of the natural samples studied and to locate the Fe oxides and oxyhydroxides within the sample's matrix, for later analysis by SEM-CL.

Synthetic Fe oxides and oxyhydroxides

Samples of goethite (SynG1, SynG2, SynG3), hematite (SynH1, SynH2, SynH3) and magnetite (SynM1) were synthesized by different methods, which are described in Appendix A. We additionally examined a commercial magnetite (SynM2). At the end of the synthesis (i.e., in all cases except the commercial magnetite), the solids were moved to 50 ml tubes, collected by centrifugation, and placed in a 0.5 or 1 mol/L HCl solution for ≈1 hour to remove remaining poorly crystalline phases. The tubes were agitated using a vortex shaker to resuspend the

products in the acid. The acidified solids were centrifuged and washed three times with doubly distilled water and dried in a vacuum oven set to 60°C for 72 hours. The dry powders were examined by both XRD and SEM. In all cases, no phase other than the Fe oxide or hydroxide of interest was identified (Figs. A1 and A2).

Natural Fe oxide and oxyhydroxide samples

Three natural goethite samples (NatG1, NatG2, NatG3), three natural hematite samples (NatH1, NatH2, NatH3), and one Ti-rich magnetite sample (NatM1) were analyzed. Brief descriptions of all natural samples are provided in Table A1. These natural samples served as comparisons to the synthetic samples, and as sources of natural spectra to the SEM-CL database. Except for NatG2, which was analyzed as a pressed pellet, natural samples were prepared and analyzed as polished sections. Prior to analysis by SEM-CL, samples were screened to verify that they contained the minerals of interest (Appendix A).

Two additional natural samples served to demonstrate the application of the methods developed in this study. These samples were analyzed as polished sections and did not undergo mineral purification prior to SEM-CL analysis. The first sample (App01) is an ooidal ironstone from the Agbaja Formation (66-72 million years old, Nupe Basin, west-central Nigeria; Umeorah, 1987). The ooids (finely laminated concentric grains) are composed of goethite and are themselves embedded in a matrix of goethite. The SEM-CL analysis of this sample was performed in mapping mode, which was possible due to the near-absence of high-luminescence minerals. The second sample (App02) is a banded iron formation from the Rapitan Group (717-661 million years ago, Mackenzie Mountains, Northwest Territories, Canada; Young, 1976). The mineralogy of this sample is simple and consists mostly of hematite and jasper. The hematite occurs in iron-rich bands alongside abundant quartz. Strong luminescence by the quartz did not

allow SEM-CL analysis of this sample in mapping mode, and we used this sample to demonstrate another mode of analysis, multiple spot-analyses.

Powder X-ray diffraction

X-ray diffractograms were obtained on a Bruker AXS diffractometer using a Cu-Kα (1.54184Å) X-ray source and a LynxEye detector. Patterns were obtained by step scanning from 15° to 50° 2θ in 0.01° increments at a scan rate of 0.35° per minute for the Mn-substituted hematite and goethite, and from 10° to 80° 2θ in 0.02° increments at a scan rate of 0.95° per minute for the other samples. The X-ray diffractograms were automatically compared with the International Center for Diffraction Data (ICDD) database and the Crystallography Open Database (COD). The unit-cell dimensions of the substituted goethite and hematite were calculated from the peak positions using a Rietveld (unit cell lattice parameter) refinement method with the MDI Jade 9 software. The peak widths were used in the Scherrer formula (Patterson, 1939) to calculate the mean crystalline dimension (MCD) of the (104) and (110) lattice planes for hematite and the (110) and (020) lattice planes for goethite. With the exception of the two samples on which we tested application of the developed SEM-CL methods, natural samples underwent a mineralogical purification step prior to XRD analysis (Appendix A), which yielded >92% of the mineral of interest and prevented the interference of high-luminescence minerals in the SEM-CL analysis.

Attenuated total reflectance Fourier transform infrared spectroscopy (ATR-FTIR)

Infrared spectra of the Mn-substituted goethite and hematite were evaluated on a Bruker ALPHA FTIR spectrometer equipped with a diamond crystal ALPHA-P ATR module. The spectral data were collected from 400 to 4000 cm^{-1} with a 4 cm^{-1} resolution. The results of 24 scans were averaged to reduce noise. The detection limit for routine analysis is ~0.1 wt%.

This is the peer-reviewed, final accepted version for American Mineralogist, published by the Mineralogical Society of America.
The published version is subject to change. Cite as Authors (Year) Title. American Mineralogist, in press.
DOI: https://doi.org/10.2138/am-2022-8843. http://www.minsocam.org/

147 **Inductively coupled plasma mass spectrometry (ICP-MS)**

148 The synthetic samples were dried in a vacuum oven overnight (at 105°C), weighed (5-10
149 milligrams) and dissolved in 3 ml of 12 M ICP-MS-grade hydrochloric acid. After complete
150 digestion, the solutions were diluted, measured on an Agilent 7700 quadrupole ICP-MS, and
151 calibrated against measurements of fresh multi-element standard on the same instrument, in the
152 same analytical session. The detection limit of the Agilent 7700 quadrupole ICP-MS is at the
153 sub-ppb range for the elements of interest.

154 **Raman microscopy**

155 Raman microscopy was applied only to the ooidal ironstone from the Agbaja Formation (sample
156 App01) to verify the Fe oxide mineralogy. Samples were analyzed by Raman using a Horiba
157 LabRAM HR Evolution spectrometer equipped with a HeCd 325-nm laser (Kimmon). The
158 system has an 800-mm focal length spectrograph with interchangeable gratings and is mounted
159 with an open-electrode, front-illuminated, cooled charge-coupled device detector. Samples were
160 placed under a modular microscope (Olympus BX-FM) with a LMU-40X-NUV
161 ×40/0.5 numerical aperture objective (Thorlabs). Samples were analyzed (532 nm excitation)
162 with a dispersive grating of 600 gr/mm. The laser spot size was typically smaller than 1 μm
163 when using the ×50 objective.

164 **Cathodoluminescence by scanning electron microscopy (SEM-CL)**

165 The SEM-CL spectra were measured on a Gatan MonoCL4 Elite system equipped with a
166 retractable diamond-turned mirror. The spectral range was set to 300-800 nm with a band pass of
167 20 nm by choosing the 150 lines/mm grating centered on 550 nm and a 1 mm entrance slit. The
168 CL system is installed on a Zeiss Gemini SEM 500, a high-resolution SEM equipped with a two-
169 mode field emission gun. Measurements were performed at 15 kV with an aperture of 60 μm in

analytical high-current gun mode. Imaging of CL spectra was performed both in 2D array mode and in multi-point mode. The pixel size and exposure time were fixed for each sample according to its CL intensity (lower intensity required larger pixel size or longer exposure time). Images were collected simultaneously using a secondary electron detector (Everhardt-Thornely).

We conducted two types of SEM-CL measurements. The first was used mainly on our synthetic minerals, in which a pellet of about 10 mg was made using a hand press (PIKE Technologies). Pellets were mounted on SEM stubs using carbon tape and coated with a layer of carbon 10 nm thick, using carbon thread evaporation (Safematic CCU-010). The second type of measurement, which was mainly applied to natural samples, was as a round, 1" polished section (Appendix A). As natural samples are usually heterogeneous, a greater number of analyses per sample were performed. To guarantee success in identifying and analyzing the minerals of interest in the polished sections, we performed powder XRD analyses on aliquots of the same rocks from which the sections were prepared. In addition, each round section was explored by SEM-EDS (Bruker X-Flash 60 mm SSD detector) to detect several suitable regions of interest, prior to examination with the SEM-CL detector (Appendix A). We find the high magnification capabilities of new SEM instruments together with the protocols for prior verification and location of the Fe oxides and oxyhydroxides to be key for the CL study of these minerals in natural materials, which often consist mainly of high-luminosity minerals such as quartz, calcite and dolomite.

All measured spectra were normalized, so that their intensity varied between zero and unity, and fit using a Matlab® program of our own development (Appendix A). The fit was composed of the minimal number of Gaussian-shaped absorption bands required to reproduce the spectra. For all three minerals studied, three Gaussians were sufficient (e.g., Fig. 1). As no CL spectra of

the Fe oxides and oxyhydroxides are available, the wavelength range allowed for the fitted Gaussian peak centers was informed by previous studies of Fe oxide photoluminescence (Shen et al., 2012; Rufus et al., 2016; Wang et al., 2018; Rufus et al., 2019) and by the spectra obtained in this study. The statistics of and covariation among the parameters of the three Gaussian bands (peak intensity, peak center wavelength in nm, full width at half-maximum in nm) were studied. Samples with low signal-to-noise ratios (e.g., when luminescence intensity was low) were excluded from the statistics. The threshold for exclusion of spectra was a sum of squared errors (SSE) between the best-fit model curve and the measured data of 0.1. Given the number of data points in a single spectrum (≈160), the SSE of threshold of 0.1 is equivalent to an average absolute error of ≈0.025 normalized intensity units at each of the individual wavelengths in the spectrum.

Results

X-ray diffraction

Our measurements confirmed the presence of the mineral of interest in all natural and synthetic samples (Fig. A1) and in the Mn-substituted goethite and hematite samples (Fig. A2). No minerals other than the minerals of interest were detectable by XRD, except in NatH1, NatH2 and NatH3, in which minor amounts of quartz were detected (Fig. A1).

The XRD patterns of the Mn-substituted samples were used to constrain the lattice parameters upon Mn incorporation. In the Mn-substituted orthorhombic goethite (n=5), the 'a' and 'c' dimensions of the unit cell decrease linearly (R^2=0.8797 and R^2= 0.9743, respectively) and the 'b' dimension increases linearly (R^2=0.9882) with increasing Mn mole % (Table 1, Fig. A3). With increasing Mn substitution for Fe, the goethite mean crystalline dimension MCD (110)

remains constant, perhaps with a slight increase (R^2=0.6334), whereas the MCD (020) decreases (R^2=0.8477). That is, goethite laths become narrower with increasing Mn substitution for Fe.

In the hexagonal hematite, the 'a' and 'c' dimensions of the unit cell increase linearly (n=5, R^2=0.8838 and R^2=0.9928, respectively) with increasing Mn substitution for Fe (Table 2, Fig. A4). Over an increase in Mn from 0 to ≈29 mole %, the 'a' and 'c' dimensions increase by ≈0.5% and ≈1.4%, respectively. The hematite MCD (104) (R^2=0.6650) was used to represent the crystal size along the 'c' axis, while the MCD (110) (R^2=0.9198) was used to represent the crystal size along the 'a'-'b' plane (Li et al., 2016). With increasing Mn substitution for Fe, the ratio MCD (104)/MCD (110) remains relatively constant (≈0.2-0.3), indicating that the crystal morphology of hematite remains generally unchanged.

We note that the relatively small number of samples (n=5) in both the Mn-substituted goethite and hematite renders the statistics of the unit cell parameters unreliable (Jenkins and Quintana-Ascencio, 2020). Hence, we advocate caution in using the unit cell parameter values inferred from our measurements, and we report R^2 simply to illustrate the linear relationship between Mn substitution and the unit cell parameters of goethite and hematite.

Fourier transform infrared spectroscopy

Goethite and hematite were positively identified in the FTIR measurements (Appendix A). Goethite was identified on the basis of the bulk O-H stretching at ≈3100 cm^{-1}, the in-plane and out-of-plane bands at ≈890 cm^{-1} and 790 cm^{-1}, respectively, and the Fe-O stretch parallel to unit cell axis **a** at ≈610 cm^{-1}. Hematite was identified on the basis of two Fe-O vibrational mode absorption bands at ≈430 and ≈530 cm^{-1}, which are perpendicular to the 'c' direction (Rendon and Serna, 1981). All goethite and hematite absorption bands become wider with increasing Mn

237 substitution for Fe (Fig. A5), as expected from the associated increase in the diversity of O-H
238 and Fe-O bonding environments.

239 **CL spectra of Fe oxides and oxyhydroxides**

240 All CL spectra of pure Fe oxides and oxyhydroxides measured in this study are available as
241 reference spectra (Supplemental file). The three examined Fe oxides and oxyhydroxide minerals
242 display distinct CL spectra (Figs. 1-3, true-color representations in Figs. A6-A8), both in the
243 wavelength of maximal emission (magnetite<goethite<hematite) and in the overall structure
244 (Fig. 2). Synthetic and natural samples of each of the individual minerals studied display broadly
245 similar spectra (Fig. 3). All spectra were deconvolved into three Gaussian bands. The center,
246 full-width at half of the maximum intensity and the maximal intensity of band *i* are denoted λ_i,
247 $FWHM_i$ and I_i, respectively.

248 A total of 1750 goethite spectra were acquired from the synthetic and natural samples (1
249 spectrum each from SynG1, SynG2, SynG3, NatG1, NatG2, NatG3, and 1744 spectra from
250 App01). Analysis of these spectra shows that goethite emission increases sublinearly with
251 wavelength from ≈350 nm, reaches a maximum between 580 and 620 nm, then decreases
252 sublinearly out to ≈850 nm (Figs. 2 and 3). Best-fit deconvolutions of goethite spectra include
253 three Gaussian components, with peak centers at λ_1=476 (±26), λ_2=596 (±30) and λ_3=685 (±38)
254 nm (average ± 2σ of 1750 synthetic and natural spectra; Figs. 1-3 and A9). The representative
255 color of goethite CL emission is yellow, with variation in the hue among samples (Fig. A6). A
256 total of 169 hematite spectra were acquired from the synthetic and natural samples (1 spectrum
257 each from SynH1, SynH2, SynH3, NatH1, NatH2, NatH3, and 163 spectra from App02).
258 Analysis of these spectra shows that hematite emission reaches a maximum between 600 and 630
259 nm. The increase in emission starts at ≈350 nm and often shows a change in the slope around

550 nm. Between 350 and 550 nm, emission increases slowly (in the synthetic samples, Figs. 2 and 3) or displays a shoulder (in the natural samples and in the Mn-substituted synthetic samples). Best-fit deconvolutions of hematite spectra include three Gaussian components centered at λ_1=≈477 (±12), λ_2=≈614 (±12) and λ_3=≈686 (±24) nm (average ± 2σ of 169 synthetic and natural spectra; Figs. 1-3 and A10). The representative color of hematite CL emission is orange, with slight variation in the hue among samples (Fig. A7).

Only three samples of magnetite were examined (two synthetic, one natural), and we do not present the statistics of Gaussian band parameters for the fits to the magnetite CL spectra. We note that magnetite exhibits the greatest variation in the emission spectrum of the studied samples. Both synthetic magnetites show a similar spectrum, with three emission bands; a strong band at λ_3=630-650 nm and two weaker bands at λ_2=≈515 and λ_1=≈455 nm (Fig. 3C), which combine into a broad spectrum with a single prominent peak. In contrast, the Ti-substituted natural magnetite is characterized by three bands: a strong band at λ_3=≈720 nm and two weaker bands at λ_2=≈560 and λ_1=≈465 nm. All bands in the natural, Ti-substituted magnetite are shifted to longer wavelengths than the synthetic magnetites, notably the higher-wavelength bands (the ≈720 and ≈560 nm bands are shifted by ≈75 and ≈45 nm, respectively). This major difference in the spectra is evident also in the real color representation (from yellow and bright green to blue, Fig. A8).

Mn-substituted Fe oxide and oxyhydroxide spectra

The CL spectra of Mn-substituted goethite and hematite show a clear change as the Mn mole % increases (Fig. 4). For goethite, the spectrum widens with increasing Mn substitution, mostly through an increase in the full width at half-maximum (FWHM) of the emission band at ≈600 nm (Fig. A11). This widening is accompanied by minor changes in the wavelength of peak

emission, which remains near 600 nm. Together with the overall symmetric widening of the spectrum with increasing Mn content, this results in very subtle blue-shifting of goethite's yellow emission (Fig. 4B). For hematite, as Mn increasingly substitutes for Fe, the spectrum widens asymmetrically. A shoulder in the left limb of the CL spectrum grows, driven by an increase in the intensity of the band centered at ≈480 nm (Fig. A11). In addition, the wavelength of peak emission decreases by ≈30 nm, and together with the greater contribution of the low-wavelength (i.e., bluer) shoulder to the total emission, this spectral shift manifests as an observable change in hematite's color of emission (Fig. 4C).

Case studies of natural samples

To test the method developed here, we analyzed Fe oxides and oxyhydroxides within a whole-rock matrix. The Agbaja ooidal ironstone (App01) contains goethite ooids embedded in a goethite matrix, with little to no high-luminescence minerals. The absence of "luminescence pollution" allowed the application of SEM-CL mapping to relate variations in the goethite properties to the petrography of the samples (Fig. 5). We analyzed 1938 points in mapping mode, 1744 of which yielded workable spectra (i.e., high enough intensity and signal-to-noise ratio). Most of the pixels that did not yield workable spectra are located at the domain edges, where concavity in the detector results in low sensitivity. The true-color SEM-CL map shows minor differences between the ooids and matrix, and more notable differences within the ooids themselves (Fig. 5). These color differences are observable even though XRD analyses of ooid and matrix material that were micro-drilled under a microscope showed no mineral other than goethite (Figs. A12 and A13). We suspected, following the SEM-CL imaging and SEM-EDS elemental mapping, that the color and spectral differences within the ooids reflect the presence of thin layers of hematite, which could not be detected by bulk XRD (Figs. A13-A15). Indeed, the

existence of thin layers of hematite within the predominantly goethite ooids were confirmed by micro-Raman spectroscopy (Fig. A16). Maps of the spectral fit parameter values accentuate the differences between the varieties of goethite present in the sample, as well as between the goethite and hematite (Fig. 5).

The banded iron formation from the Rapitan Group (App02) contains, in addition to hematite, an abundance of high-luminescence minerals, mostly quartz, but also small amounts of calcium phosphate and calcium-magnesium carbonate minerals (Figs. A12, A17 and A18). Due to the masking of the Fe oxide CL emission by the presence of these much more luminescent minerals, SEM-CL mapping is not possible in this case. Instead, we performed multiple SEM-CL point-analyses to identify variations in the spectra of hematite. We analyzed a total of 218 points, which were selected on the basis of SEM-EDS (high Fe, low Si) and SEM-CL mapping (low luminescence, indicating Fe-bearing minerals). Of these points, 163 yielded workable spectra, and hematite was the only Fe oxide or oxyhydroxide identified in these spectra. Hematite emission color variations were small, but variations in some of the spectral fit parameters were notable (Fig. 6).

Discussion

Investigation of the relative timing and conditions of growth and recrystallization of Fe oxides and oxyhydroxides (and other opaque minerals) in geologic samples is complicated by the limitations of existing petrographic techniques. The SEM-CL methods developed and presented here may allow such investigations. Furthermore, these techniques may allow application of CL to other minerals that have not been amenable to study by traditional OM-CL. Coupled with SEM-EDS, SEM-CL is a nondestructive tool for in situ mineralogical identification, chemical characterization and petrographic study of such minerals. As such, SEM-EDS-CL has

329 advantages over methods that require the samples to be powdered (e.g., powder XRD), leading to
330 loss of spatial context, as well as advantages over methods that provide only mineralogical
331 information (e.g., micro-Raman) or only chemical information (e.g., XRF).

332 Two scales of difference are evident among the SEM-CL spectra obtained (Figs. 1-4, A6-A8).
333 The first is the prominent difference between the spectra of hematite, goethite and magnetite,
334 which may be used for mineral identification purposes. The second involves more subtle
335 differences among spectra of the same mineral, which are caused by the multiple controls on the
336 mineral SEM-CL spectrum. Such spectral differences may be used to study episodes of mineral
337 formation or recrystallization, or to extract information about variations in the controls on the
338 SEM-CL spectrum. In this context, we explore Mn substitution and the mineral synthesis method
339 (an imperfect proxy for the formation mechanism) as such controls. Among other factors,
340 solution composition and pH, formation temperature, formation mechanism, and precipitation
341 rate all have the capacity, in theory, to affect the extrinsic or intrinsic luminescence centers of a
342 mineral.

343 We emphasize that the spectral deconvolution algorithm yields best-fit positions, widths and
344 intensities of Gaussian bands, but that the physical meaning of these bands is unclear. We
345 discuss possible explanations for the Gaussian components of the spectrum and show the utility
346 of the spectral deconvolution in accentuating differences between occurrences of the same
347 mineral. However, additional experimental and theoretical work is required before physical
348 mechanisms may be confidently assigned to variations in the band parameters.

349 **The SEM-CL spectra of goethite, hematite, and magnetite**

350 Goethite, hematite, and magnetite display distinct SEM-CL emission spectra (Figs. 1-3).
351 Differences between mineral CL emission spectra are typically attributed to the crystal properties

and structure (Boggs and Krinsley, 2006). Although SEM-CL emission by Fe oxides and oxyhydroxides has never been studied systematically, inferences may be made from photoluminescence (PL) and visible and near-infrared (Vis-NIR) studies. Goethite, hematite and magnetite are characterized by band gaps of 2.1, 2.2 and 2.5 eV, respectively (Cornell and Schwertmann, 2003; Taufiq et al., 2018). These band gaps correspond to a wavelength of 590, 560 and 495 nm, respectively, imposing lower limits on the wavelength of emission (upper limits on the energy) from these minerals. Capture in luminescence centers of the electrons decaying from an excited state to the ground state increases the emission wavelength, typically by no more than a few tens of nm. For example, the PL emission spectrum of hematite nanoparticles includes a major band at 575 nm (compared to the band gap at 560 nm), which has been attributed to band edge emission (Rufus et al., 2019). Similarly, the strongest SEM-CL emission bands that we observed in hematite (λ_2 of ≈615 nm, band gap at 560 nm), goethite (λ_2 of ≈600 nm, band gap at 590 nm) and magnetite (λ_2 of ≈515 nm, band gap at 495 nm) may be explained by band edge emission. The shift in the band position is to longer wavelengths, as expected. However, other than for hematite, the apparent shift is smaller than the 20-nm spectral resolution of our CL spectra and is therefore uncertain.

In studies of hematite PL, the emission band at 400-500 nm has been attributed to the crystal field splitting of an FeO_6 octahedron (Pal et al., 2014). Informed by this work, we suggest that the low-wavelength SEM-CL emission bands observed here (hematite, goethite and magnetite λ_1 of ≈477, ≈475 and 456 nm, respectively) are similar phenomena. According to crystal field theory, the interaction between a transition metal and ligands arises from the attraction between the positively charged metal cation and the negative charge on the non-bonding electrons of the ligand. A change in the relative proportions of different cations in octahedral sites, as in our Mn-

375 substituted hematite and goethite, is expected to manifest as a change in the parameters of the
376 emission band at ≈450-480 nm. Indeed, in addition to changes in the other spectral components
377 (discussed in Section 4.3), substitution of Mn for Fe in the FeO_6 octahedron invoked a shift of
378 ≈30 nm in the peak center and an approximate doubling in the intensity of the 450-480 nm
379 emission band. Our third Gaussian fit component, with an emission peak at 680-720 nm, is
380 similar to a PL emission band at the 688 nm, which has been attributed to shifts in the band edge
381 emission in nanoscale hematite particles, or to surface defects (Rufus et al., 2016).

382 Interestingly, Vis-NIR reflectance spectra also share similarities with SEM-CL spectra,
383 possibly since electronic transitions contribute to both (exclusively to SEM-CL spectra and
384 together with vibrational transitions to Vis-NIR spectra). Given the lower energy of excitation
385 (i.e., visible light), electronic transitions are less dominant in Vis-NIR reflectance spectra than in
386 their SEM-CL counterparts. Peak emission in the SEM-CL spectra (~600-650 nm for goethite,
387 hematite and magnetite) appears as a shoulder in these minerals' Vis-NIR reflectance spectra,
388 which peak at longer wavelengths (~750-800 nm; Figure A19). Further studies are needed to
389 systematically explore similarities and differences between the SEM-CL and Vis-NIR
390 reflectance spectra.

391 The above attribution of spectral components to different phenomena is supported by
392 differences in the SEM-CL spectra of natural and synthetic samples. The natural samples
393 generally display a more intense 400-500 nm emission band (e.g., Fig. 3) relative to the synthetic
394 samples. If this band is due to crystal field splitting of an octahedrally coordinated metal (Fe or
395 substituting cation), as suggested in previous work (Pal et al., 2014), the enhanced emission may
396 be explained by metal substitution for Fe in the mineral lattice. Such substitution is common in
397 natural environments (e.g., Trolard et al., 1995), and is expected to be minor in our synthetic

398 samples. Cation substitution for Fe in natural samples is also consistent with the broader
399 emission spectra of these samples relative to synthetic samples.

400 It should be noted that previous research on other minerals suggests that CL spectral
401 differences are also expected to arise from other factors, such as the mineral's formation pH,
402 grain size, crystal-growth parameters, and parent-solution chemistry (e.g., Ramseyer and Mullis,
403 1990), and that both intrinsic and extrinsic defects can affect the SEM-CL characteristics of a
404 mineral (Rusk, 2012; Frelinger et al. 2015). To fully comprehend the controls on the SEM-CL
405 spectra of Fe (oxyhydr)oxides, systematic experimental work and analyses of natural samples are
406 required.

407 **Differences among SEM-CL spectra of the same mineral**

408 Differences among the SEM-CL spectra of samples of the same mineral are smaller than
409 differences between the different Fe oxides and oxyhydroxides. Nevertheless, given the need for
410 a tool to distinguish between oxides formed in different mineralization conditions or episodes,
411 these small differences may be harnessed for several geochemical or petrographic applications.
412 With the exception of NatM1, which will be discussed below, the studied minerals exhibit only
413 minor variations in the visible emission color (Figs. A6-A8). Therefore, it is likely that these Fe
414 oxides and oxyhydroxides under traditional OM-CL apparatus, would yield little insight into the
415 (re)mineralization history of the studied samples. We propose that such insight may be gained by
416 the ability to quantitatively analyze the full spectra of the Fe oxides and oxyhydroxides, acquired
417 by SEM-CL on small spatial scales (nm to μm).

418 The spectrum of SynG1 is shifted to higher wavelength (maximal emission at ≈617 nm),
419 relative to the spectra of SynG2 and SynG3 (maximal emission at ≈604 and ≈595 nm,
420 respectively). In addition, SynG1 displays a less pronounced shoulder around 450 nm than

SynG2 and SynG3 (Fig. 3). Differences in formation temperature between SynG1 (60°C) and SynG2 (70°C) are minor, as are differences in their chemical composition (Table A3), suggesting that these factors did not cause the spectral differences. Furthermore, SynG2 was precipitated from a ferric-nitrate solution, whereas SynG1 and SynG3 were precipitated from a ferric-chloride solution, suggesting that the major element composition of the solutions did not cause the spectral differences. The synthesis of SynG1 did differ from those of SynG2 and SynG3 in its pH (≈7 as opposed to ≈13.6 and ≈11, respectively). Irrespective of the exact mechanism by which the synthesis pH affected the spectrum, the existence of the spectral differences suggest sensitivity to this parameter.

The samples NatG1 and NatG3 both come from ooids that formed in a shallow marine setting characterized by venting of hydrothermal fluid (Table A1). The measured temperature of the sediments at the NatG1 formation site is 42°C (Heikoop et al., 1996). The formation temperature of NatG3 was not directly measured. However, the temperature of the vented fluids at the collection site range from 40 to 140 °C (Di Bella et al., 2019). Despite a distance of ≈12000 km between the formation sites of these ooids, NatG1 and NatG3 exhibit similar SEM-CL spectra (Figs. 3 and A6). The spectral similarity between these goethite samples may be related to the similar chemical composition (seawater) and temperature of the solutions from which they formed. In such similar formation environments, the amount and type of elemental substitutions in the goethite and the compounds sorbed to its surface are expected to be similar. Indeed, the two samples' SEM-EDS maps (Figs. A20 and A21) show similar elemental compositions (notably, Fe, Mg, Cl, S, K, P). The presence of poorly crystalline Fe hydroxides (ferrihydrite) in both samples, together with their similar chemistry and depositional environment, suggests that both were formed by transformation of ferryhydrite into goethite at or near the sediment surface.

444 The spectrum of NatG2 differs subtly from those of the hydrothermally-influenced goethite
445 samples (NatG1 and NatG3). Specifically, the spectrum of NatG2 displays a maximum at ≈613
446 nm, compared with ≈591 nm in NatG1 and NatG3, and a less pronounced shoulder around 450
447 nm (Figs. 3 and A6). The less pronounced shoulder may be related to a lesser degree of
448 elemental substitution in NatG2, which is an oxidation product of pyrite (FeS_2) rather than a
449 precipitate from a seawater-like solution. The higher wavelength of emission may be related to
450 the existence of slightly different luminescence centers, which decrease the emission peak
451 energy from the band gap by different amounts. We note that the overall differences of the
452 spectrum of NatG2 from those of NatG1 and NatG3 are qualitatively similar to the proposed pH-
453 related differences between the spectrum of SynG1 and those of SynG2 and SynG3 (Fig. 3A). As
454 pyrite oxidation often results in acidification of the solutions involved, it is possible that the
455 spectrum of NatG2 reflects formation at a lower pH than NatG1 and NatG3, which formed in
456 seawater-like solutions. Irrespective of the exact reasons for the spectral differences between
457 NatG2 and the other natural goethite samples, the existence of these differences suggests that
458 different formation pathways and environments may result in slightly different spectra of the
459 same mineral.

460 The SEM-CL spectrum of SynH3 is broadly similar to those of SynH1 and SynH2 (Fig. 3B), as
461 expected given their similar mineralogy, and despite the formation of SynH3 by thermal
462 dehydration of goethite (at 500°C) rather than aging of ferrihydrite (as in the case of SynH1 and
463 SynH2). Specifically, all three synthetic hematite samples display very similar spectra between
464 ≈400 and ≈600 nm. At the higher wavelengths, the decrease in emission intensity in SynH1 and
465 SynH2 is concave upwards, whereas in SynH3 it is sub-linear, suggesting a lesser importance of
466 the band at ≈700-750 nm. Given suggestions that this spectral feature may be related to surface

467 defects (Rufus et al., 2016), it is possible that the heating to 500°C resulted in annealing of
468 defects and a weakening of the associated band edge emission.

469 The natural hematite spectra are very similar at wavelength >≈600 nm but differ at lower
470 wavelengths (Fig. 3B). Specifically, there is high variability in the intensity of the emission
471 shoulder at ≈450 nm. The physical environment of formation in unlikely to be the cause of these
472 spectral differences, given that NatH1 and NatH2, both of which come from ooidal ironstones of
473 broadly similar age (i.e., formed from ancient seawater with a similar chemical composition),
474 display maximally different spectra (Fig. 3B). As the band at ≈450 nm is suggested to relate to
475 metal substitution for Fe in the octahedral sites, it is possible that the observed spectral
476 differences arise from differences in trace metal concentrations in these samples (Figs. A22-
477 A24).

478 The spectra of the synthetic magnetite samples, SynM1 and SynM2 differ substantially in the
479 wavelength of maximal emission (≈536 and ≈599 nm, respectively), and these differences may
480 be related to different synthesis conditions (Fig. 3C). SynM1 formed by precipitation from
481 synthetic seawater, whereas SynM2 is a commercial reagent with a synthesis method unknown to
482 us, but which is unlikely to be precipitation in seawater-like solutions. The spectral differences
483 are substantial enough to manifest as an observable emission color difference (Fig. A8).

484 The spectrum of NatM1 differs from all other spectra in this study, in that it displays two major
485 peaks, the larger of which occurs at ≈725 nm (Figs. 3C and A8). In the absence of this peak, the
486 spectrum of NatM1 would display relatively intense emission at ≈450 nm, and this may be
487 related to its high Ti content, although more systematic investigations are required to verify this
488 suggestion. (Fig. A25). However, the surface of NatM1 also displays clear etch pits (Fig. 7), and

this may be the cause of the intense emission at ≈725 nm (Rufus et al., 2016), which dominates the spectrum.

Mn-substituted goethite and hematite

To explore the effects of metal substitution for Fe on the SEM-CL spectrum, we synthesized and analyzed Mn-substituted goethite and hematite. We studied the Mn-substituted goethite and hematite by FTIR and XRD to constrain structural changes upon Mn-substitution. Previous studies have shown that Mn is incorporated into the goethite structure in trivalent form (Mn^{3+}), even if the Mn is present in solution in divalent form (Mn^{2+}; Sileo et al., 2001), suggesting oxidation on the mineral surface. The crystal radius of octahedrally coordinated Mn^{3+} is larger than that of Fe^{3+} (0.72 and 0.69 Å, respectively; Shannon, 1976), and substitution of Mn^{3+} for Fe^{3+} is expected to result in larger octahedra in both goethite and hematite. The XRD results show clear changes in the unit cell dimensions with increasing Mn concentrations (Table 1, Fig. A3), which are plausibly explained by Mn substitution for Fe in the octahedral sites of goethite and hematite. In goethite, the observed shortening of the 'a' and 'c' axes and lengthening of the 'b' axis with increasing Mn concentrations (Table 1, Fig. A3), are consistent with a gradual change in the structure from goethite to the Mn-oxide groutite (α-FeOOH to α-MnOOH; Stiers and Schwertmann, 1985; Ebinger and Schulze, 1989). Lengthening does not occur along all crystal axes, as octahedra in goethite share vertices or edges, and some of the effects of larger octahedra are accommodated by changes in the angles between the octahedra. In hematite, we observe a lengthening of both the 'a' and 'c' axes with increasing Mn concentration (Table 2, Fig. A3). Such a lengthening is expected given that octahedra share faces in hematite, limiting the ability of the crystal structure to accommodate larger octahedra, other than by an increase in cell size.

512 The above changes in the goethite and hematite lattice with increasing Mn substitution for Fe
513 translate into changes in the SEM-CL spectra (Fig. 4). In goethite, a slight increase in the relative
514 intensity of the band at ≈450 nm is observed, but this does not result in a major change in the
515 spectrum shape. Instead, the goethite spectrum appears to widen in an approximately symmetric
516 manner (Fig. 4B). This broadening is observed mostly in bands 2 and 3 (Fig. A11), which are
517 suggested to be related to intrinsic luminescence centers (e.g., Pal et al., 2014). As such, the
518 broadening may be the outcome of an increase in the diversity of luminescence centers, related to
519 the accommodation of the larger MnO_6 octahedra by changes in the angles between the
520 octahedra. In hematite, the increase in the intensity of the band at ≈450 nm is more pronounced
521 (Fig. A11D), and in addition to broadening, the spectrum gains intensity at low wavelengths
522 relative to the Mn-free hematite. This results in a noticeable change in the color of emission,
523 from orange in the Mn-free hematite to light yellow in the hematite with 28.5 mole % Mn (Fig.
524 4C). Broadening in the FTIR spectra of both goethite and hematite is observed (Fig. A5), likely
525 associated with an increase in the diversity of O-H and Fe-O bonding environments, and
526 consistent with our explanation for the peak broadening observed in the SEM-CL spectra.

527 Our results raise the possibility of using SEM-CL not only for identification of Fe oxides and
528 oxyhydroxides, but also to detect varieties of Fe (oxyhydr)oxides within the same rock or soil
529 sample that formed in solutions with a different chemical composition. For example, Mn
530 concentrations in groundwater solutions may differ from those in seawater-derived porewater,
531 and hematite formed from these two different solutions is, therefore, expected to differ in its
532 SEM-CL spectrum (Fig. 4), allowing distinction between early diagenetic and late-stage
533 hematite. Similarly, previous work on natural goethite samples (Fitzpatrick and Schwertmann,
534 1982) showed that Al substitution for Fe in goethite can serve as an indicator of the mineral

formation setting. Low Al mole % in goethite is common in hydromorphic (characterized by excess water) soils and carbonate-rich environments (including marine settings), whereas high Al mole % is typical in non-hydromorphic, highly weathered environments. If Al substitution for Fe in the goethite lattice affects the emission spectrum of goethite, SEM-CL could be used as an in situ, non-destructive method to identify goethite and distinguish a probable marine origin from a terrestrial weathering origin. The development of SEM-CL as a means of detecting polygenicity and provenance of Fe (oxyhydro)oxides through the effect of impurities on the luminescence spectrum requires further experimental and theoretical work.

Natural case studies

The Agbaja ooidal ironstone (App01). In the sample from the Agbaja ooidal ironstone (App01), both the yellow matrix and the black lustrous ooids are made of goethite (Fig. A13). The SEM-EDS maps show that the Fe is present throughout the sample, Si is present almost exclusively in the matrix, and the Al concentration in the matrix is higher overall than in the ooids, especially near the ooid rims. In addition, the maps show alternating Al- and P-rich and Al- and P-poor layers within the ooids.

The SEM-CL map of an ooid and its neighboring matrix in App01 shows color variations that are unexpected given the monomineralic nature of these samples, as constrained by XRD (Fig. A13). Surprisingly, the greatest differences in SEM-CL color are not observed between the ooid and the matrix, but within the ooid itself. The orange banding, which appears to associate with more porous, Al- and P-poor bands in the ooid (Fig. 5), is reminiscent of the emission color of hematite (Figs. 1, 4 and A7), though no hematite was detected by XRD. Indeed, micro-Raman analysis of selected points in the ooid and matrix (marked as 1-3 in Fig. 5) verifies the existence of hematite, as suggested by the SEM-CL map. This demonstrates the utility of SEM-CL in in

558 situ distinction between minerals with an abundance too low to be detected by XRD and in close
559 spatial proximity.

560 In combination with SEM-EDS, the mineral identification capabilities of SEM-CL allow
561 distinction between two different phases of goethite formation—under relatively Al-poor
562 conditions during formation of the ooids and more Al-rich conditions during formation of
563 goethite in the matrix. The combined chemical-mineralogical information shows that the Al is
564 present in association with the goethite itself, rather than in silicates. The low concentrations of
565 Al and P in the microns-thick hematite layers suggest that transformation of goethite to hematite
566 occurred in the presence of fluids that transported the Al and P away. If this were not the case,
567 the concentrations of these elements in the hematite and goethite would be similar, or there
568 would be an enrichment of these elements in the interface between the goethite and hematite.
569 The Al enrichment observed in the matrix goethite in immediate contact with the ooid rims may
570 be related to the Al excluded from the hematite layers in the ooid.

571 In addition to the emission color differences that seem to be related to different mineralogy
572 (goethite vs. hematite), subtle true color variations are observed within the goethite itself (Fig. 5).
573 These differences are more pronounced between the ooid and matrix, and they may be related to
574 the different concentrations of Al, Si, and Ti in these components of the rock, as revealed by the
575 SEM-EDS map (Figs. A14 and A15). As discussed above, the presence of impurities is expected
576 to affect the amount and nature of extrinsic luminescence centers. The emission color variations
577 within the goethite in the ooids are almost imperceptible to the human eye, giving the impression
578 that the goethite in the ooids is homogeneous. However, the spectral deconvolution reveals easily
579 observed patterns in some of the spectral parameters, which allow even further classification of
580 the goethite (white rectangle in Fig. 5). Hence, emission color and spectral parameter maps

obtained by SEM-CL may provide spatial information about episodes of mineralization and inhomogeneity within single minerals.

The Rapitan iron formation (App02). Due to the presence of high-luminescence minerals in close association with Fe oxides and oxyhydroxides, it is not always possible to apply SEM-CL in mapping mode, as we did in App01. To develop an application of SEM-CL for such samples, we studied the Rapitan iron formation (App02), which is composed mostly of hematite and jasper (quartz with an Fe(III) impurity), with minor amounts of calcium phosphate and calcium-magnesium carbonate minerals (Figs. A17-A18). The proximity of quartz and calcium phosphate to the hematite in the Rapitan iron formation samples does not allow application of SEM-CL in mapping mode. Instead, we performed 218 spot analyses, which yielded 163 workable spectra (i.e., with a high enough signal-to-noise ratio).

The range of variation in the emission color and spectral parameters within the Rapitan samples (Fig. 6) is comparable to the variation observed in the hematitic parts of the Agbaja ooids (Fig. 5). It is difficult to confidently explain this variation (e.g., variable degrees of substitution of metals for Fe in the hematite), and we note that previous work, based on petrographic relationships, has suggested that the Rapitan iron formation is composed of no fewer than five types of hematite (Klein and Beukes, 1993). Though petrographic relationships observed in our samples indicate a single, early origin for the hematite, it is possible that multiple episodes of mineralization are documented by the SEM-CL spectral variation we observe. Regrettably, we did not obtain information about the location of the point analyses. We suggest that coupled spectral-spatial data (point SEM-CL spectra + x-y coordinates) would allow the display of emission color or spectral parameters overlaid on an image of the sample (e.g., as

603 colored markers), and that this mode of display could reveal spatial patterns in the hematite
604 SEM-CL spectra.

605 **Implications**

606 Means for non-destructive, coupled, in situ characterization of Fe (oxyhydr)oxide chemical
607 composition, mineralogy, and crystallinity, as well as the degree of preservation and alteration
608 history of these minerals in natural samples have been lacking. We bridged this gap by
609 developing methods for analyzing Fe (oxyhydr)oxides by SEM-CL. We showed that hematite,
610 goethite and magnetite have unique SEM-CL spectra, allowing identification of these minerals
611 and possibly others. Furthermore, we found that the mineral-specific spectrum varies slightly,
612 but meaningfully, from sample to sample, plausibly due to differences in the conditions of
613 mineral formation. For example, the spectra of both goethite and hematite change with
614 increasing substitution of Mn for Fe, and it is likely that substitution of other cations or anions in
615 the (oxyhydr)oxide structure would similarly affect the SEM-CL spectrum. Thus, the chemical
616 composition of the fluids from which the Fe (oxyhydr)oxides formed is expected to affect their
617 SEM-CL spectra. Spectral differences are also expected in response to formation pH and grain
618 size, among other possible parameters of the mineral's formation environment. Systematic
619 experimental work and analyses of natural samples are required to fully understand the controls
620 on the SEM-CL spectra of Fe (oxyhydr)oxides, but even without complete knowledge of these
621 controls, our findings suggest the potential of SEM-CL for identification of episodes or
622 generations of mineralization in natural samples. Indeed, application of the newly developed
623 methods to two natural samples revealed mineralogical transformations that were undetected by
624 other techniques, as well as spectral differences within Fe (oxyhydr)oxides, perhaps suggesting
625 multiple episodes of mineral formation or alteration that were otherwise difficult to distinguish.

626 Applications of Fe-oxide SEM-CL in robotic exploration of planetary surfaces may be more
627 difficult due to the interference of high-luminescence minerals and the necessity of performing
628 the analysis under vacuum. We suggest that like the application of SEM-CL to geologic samples,
629 this approach may be used for non-destructive, in situ study of the chemistry, mineralogy and
630 crystallinity of a wide range of natural and manufactured Fe oxides and oxyhydroxides.
631 Applications that come to mind include detection of impurities, defects or variations in
632 crystallinity in superconductor materials. Lastly, our results suggest the potential of SEM-CL
633 techniques for the study of other low-luminescence, Fe-bearing minerals, such as Fe sulfides
634 (e.g., pyrite, pyrrhotite) and Fe silicates (e.g., glauconite, berthierine).

635 **Acknowledgement**

636 I.H. acknowledges a Starting Grant from the European Research Council (OOID No. 755053).
637 We thank Yanay Toren for labwork, Ishai Dror for ICP-MS guidance and support, Yishay
638 Feldman for help with the Jade software, Michal Sela-Adler for help with magnetite synthesis
639 and Asaf Nissenbaum for assistance with FTIR measurements. We thank Francesco Italiano and
640 Marcella Di Bella for providing us with the sediments from which we extracted NatG3 and
641 NatM1. We thank Andrey Bekker for providing us with samples of the Agbaja ironstone and the
642 Rapitan iron formation.

643 **References**

644 Ahn J.H. and Buseck P.R. (1990) Hematite nanospheres of possible colloidal origin from a
645 Precambrian banded iron formation. Science 250, 111–113.

646 Barker C.E., Burruss R.C., Kopp O.C., Machel H.G., Marshall D.J., Wright P., Colbum H.Y.,
647 Machel H.G. and Burton E.A. (1991) Factors Governing Cathodoluminescence in Calcite
648 and Dolomite, and their Implications for Studies of Carbonate Diagenesis. In Luminescence
649 Microscopy and Spectroscopy Qualitative and Quantitative Applications Special
650 Publications of SEPM. pp. 37–57.

651 Bekker A., Slack J.F., Planavsky N.J., Krapež B., Hofmann A., Konhauser K.O. and Rouxel O.J.
652 (2010) Iron Formation: The Sedimentary Product of a Complex Interplay among Mantle,
653 Tectonic, Oceanic, and Biospheric Processes. Economic Geology. 105, 467–508.

654 Boggs S. and Krinsley D. (2006) Application of Cathodoluminescence Imaging to the Study of
655 Sedimentary Rocks., Cambridge University Press, Cambridge, UK.

656 Cornell R.M. and Schwertmann U. (2003) The Iron Oxides: Structure, Properties, Reactions,
657 Occurrences and Uses, 2nd ed., John Wiley & Sons.

658 Craddock P.R. and Dauphas N. (2011) Iron and carbon isotope evidence for microbial iron
659 respiration throughout the Archean. Earth and Planetary Science Letters. 303, 121–132.

660 Črne A.E., Melezhik V.A., Lepland A., Fallick A.E., Prave A.R. and Brasier A.T. (2014)
661 Petrography and geochemistry of carbonate rocks of the Paleoproterozoic Zaonega
662 Formation, Russia: Documentation of ^{13}C-depleted non-primary calcite. Precambrian
663 Research. 240, 79–93.

664 Di Bella M., Sabatino G., Quartieri S. and Ferretti A. (2019) Modern Iron Ooids of
665 Hydrothermal Origin as a Proxy for Ancient Deposits. Scientific Reports 9, 1–9.

Ebinger M.H. and Schulze D.G. (1989) Mn-substituted goethite and Fe-substituted groutite synthesized at acid pH. Clays and Clay Minerals. 37, 151–156.

Fitzpatrick R.W. and Schwertmann U. (1982) Al-substituted goethite- An indicator of pedogenic and other weathering environments in South Africa. Geoderma 27, 335–347.

Frelinger, S. N., Ledvina, M. D., Kyle, J. R., & Zhao, D. (2015). Scanning electron microscopy cathodoluminescence of quartz: Principles, techniques and applications in ore geology. Ore Geology Reviews, 65, 840-852.

Frimmel H. (1997) Detrital origin of hydrothermal Witwatersrand gold—a review. Terra Nova. 9, 192–197.

Galili N., Shemesh A., Yam R., Brailovsky I., Sela-Adler M., Schuster E.M., Collom C., Bekker A., Planavsky N., Macdonald F.A., Préat A., Rudmin M., Trela W., Sturesson U., Heikoop J.M., Aurell M., Ramajo J. and Halevy I. (2019) The geologic history of seawater oxygen isotopes from marine iron oxides. Science 365, 469–473.

Goldstein, J. I., Newbury, D. E., Michael, J. R., Ritchie, N. W., Scott, J. H. J., and Joy, D. C. (2017) Scanning electron microscopy and X-ray microanalysis. Springer.

Heikoop J.M., Tsujita C.J., Risk M.J., Tomascik T. and Mah A.J. (1996) Modern iron ooids from a shallow-marine volcanic setting: Mahengetang, Indonesia. Geology 24, 759–762.

Heimann A., Johnson C.M., Beard B. L., Valley J. W., Roden E. E., Spicuzza M. J. and Beukes N. J. (2010) Fe, C, and O isotope compositions of banded iron formation carbonates demonstrate a major role for dissimilatory iron reduction in ~2.5Ga marine environments. Earth and Planetary Science Letters. 294, 8–18.

Holland H.D. (1984) The chemical evolution of the atmosphere and oceans., Princeton University Press, Princeton, NJ.

Howie, R. A., Zussman, J., & Deer, W. (1992). An introduction to the rock-forming minerals (p. 696). London, UK: Longman.

Hug S.J. (1997) In situ fourier transform infrared measurements of sulfate adsorption on hematite in aqueous solutions. Journal of colloid and interface science. 188, 415–422.

Jenkins, D. G., and Quintana-Ascencio, P. F. (2020). A solution to minimum sample size for regressions. PloS one, 15(2), e0229345.

Klein C. and Beukes N.J. (1993) Sedimentology and geochemistry of the glaciogenic late Proterozoic Rapitan iron-formation in Canada. Economic Geology. 88, 542–565.

Konhauser K.O., Planavsky N.J., Hardisty D.S., Robbins L.J., Warchola T.J., Haugaard R., Lalonde S.V., Partin C.A., Oonk P.B.H.H., Tsikos H., Lyons T.W., Bekker A. and Johnson C.M. (2017) Iron formations: A global record of Neoarchaean to Palaeoproterozoic environmental history. Earth-Science Reviews. 172, 140–177.

Li W., Liang X., An P., Feng X., Tan W., Qiu G., Yin H. and Liu F. (2016) Mechanisms on the morphology variation of hematite crystals by Al substitution: The modification of Fe and O reticular densities. Scientific Reports. 6, 1–10.

Morris, R. V., Lauer Jr, H. V., Lawson, C. A., Gibson Jr, E. K., Nace, G. A., & Stewart, C. (1985) Spectral and other physicochemical properties of submicron powders of hematite (α-Fe2O3), maghemite (γ-Fe2O3), magnetite (Fe3O4), goethite (α-FeOOH), and lepidocrocite (γ-FeOOH). Journal of Geophysical Research: Solid Earth, 90(B4), 3126-3144.

Pal M., Rakshit R. and Mandal K. (2014) Facile functionalization of Fe_2O_3 nanoparticles to induce inherent photoluminescence and excellent photocatalytic activity. Applied Physics Letters. 104, 233110.

Patterson A.L. (1939) The scherrer formula for X-ray particle size determination. Physical

712 Review. 56, 978–982.

713 Pirard, E., and Lebichot, S. (2004) Image analysis of iron oxides under the optical microscope.
714 Applied Mineralogy: Developments in Science and Technology, 153-156.

715 Poulton S.W. and Canfield D.E. (2005) Development of a sequential extraction procedure for
716 iron: Implications for iron partitioning in continentally derived particulates. Chemical
717 Geology. 214, 209–221.

718 Ramseyer, K., and Mullis, J. (1990) Factors influencing short-lived blue cathodoluminescence of
719 alpha-quartz. American Mineralogist, 75(7-8), 791-800.

720 Rasmussen B., Muhling J.R., Suvorova A. and Krapež B. (2016) Dust to dust: Evidence for the
721 formation of "primary" hematite dust in banded iron formations via oxidation of iron
722 silicate nanoparticles. Precambrian Research. 284, 49–63.

723 Rendon J.L. and Serna C.J. (1981) IR spectra of powder hematite: effects of particle size and
724 shape. Clay Minerals. 16, 375–382.

725 Rufus A., Sreeju N. and Philip D. (2019) Size tunable biosynthesis and luminescence quenching
726 of nanostructured hematite (α-Fe_2O_3) for catalytic degradation of organic pollutants. Journal
727 of Physics and Chemistry of Solids 124, 221–234.

728 Rufus A., Sreeju N. and Philip D. (2016) Synthesis of biogenic hematite (α-Fe_2O_3) nanoparticles
729 for antibacterial and nanofluid applications. RSC Advances. 6, 94206–94217.

730 Rusk, B. (2012) Cathodoluminescent textures and trace elements in hydrothermal quartz. In
731 Quartz: deposits, mineralogy and analytics (pp. 307-329). Springer, Berlin, Heidelberg.

732 Scheinost, A. C., Chavernas, A., Barrón, V., and Torrent, J. (1998). Use and limitations of
733 second-derivative diffuse reflectance spectroscopy in the visible to near-infrared range to
734 identify and quantify Fe oxide minerals in soils. Clays and Clay Minerals, 46(5), 528-536.

735 Schwertmann U. and Cornell R.M. (1991) Iron oxides in the laboratory : preparation and
736 characterization., Wiley-VCH, New York.

737 Shannon R.D. (1976) Revised effective ionic radii and systematic studies of interatomic
738 distances in halides and chalcogenides. Acta Crystallographica Section A. 32, 751–767.

739 Shen S., Jiang J., Guo P., Kronawitter C.X., Mao S.S. and Guo L. (2012) Effect of Cr doping on
740 the photoelectrochemical performance of hematite nanorod photoanodes. Nano Energy 1,
741 732–741.

742 Sileo E.E., Alvarez M. and Rueda E.H. (2001) Structural studies on the manganese for iron
743 substitution in the synthetic goethite - Jacobsite system. International Journal of Inorganic
744 Materials. 3, 271–279.

745 Šima J. (2015) (Non)luminescent properties of iron compounds. Acta Chimica Slovaca.8, 126–
746 132.

747 Sperling E.A., Wolock C.J., Morgan A.S., Gill B.C., Kunzmann M., Halverson G.P., Macdonald
748 F.A., Knoll A.H. and Johnston D.T. (2015) Statistical analysis of iron geochemical data
749 suggests limited late Proterozoic oxygenation. Nature 523, 451–454.

750 Šťastná A. and Přikryl R. (2009) Decorative marbles from the Krkonoše-Jizera Terrane
751 (Bohemian Massif, Czech Republic): Provenance criteria. International Journal of Earth
752 Sciences. 98, 357–366.

753 Stiers W. and Schwertmann U. (1985) Evidence for manganese substitution in synthetic goethite.
754 Geochimica et Cosmochimica Acta. 49, 1909–1911.

755 Stolper D.A. and Keller C.B. (2018) A record of deep-ocean dissolved O_2 from the oxidation
756 state of iron in submarine basalts. Nature 553, 323–327.

757 Tarashchan A.N. and Waychunas G. (1995) Interpretation of luminescence spectra in terms of

band theory and crystal field theory. Sensitization and quenching, photoluminescence, radioluminescence, and cathodoluminescence. Advanced Mineralogy. 2, 124–135.

Taufiq A., Yuliantika D., Hariyanto Y.A., Hidayat A., Bahtiar S., Mufti N. and Hidayat N. (2018) Effect of Template on Structural and Band Gap Behaviors of Magnetite Nanoparticles. Journal of Physics: Conference Series. 1093, 012020.

Torrent, J., and Barrón, V. (2002) Diffuse reflectance spectroscopy of iron oxides. Encyclopedia of surface and Colloid Science, 1, 1438-1446.

Trolard F., Bourrie G., Jeanroy E., Herbillon A.J. and Martin H. (1995) Trace metals in natural iron oxides from laterites: A study using selective kinetic extraction. Geochimica et Cosmochimica Acta. 59, 1285–1297.

Umeorah E. M. (1987) Depositional environment and facies relationships of the Cretaceous ironstone of the Agbaja Plateau, Nigeria. J. African Earth Sci. 6, 385–390.

Wang T., Jiang Z., Chu K.H., Wu D., Wang B., Sun H., Yip H.Y., An T., Zhao H. and Wong P.K. (2018) X-Shaped α-FeOOH with Enhanced Charge Separation for Visible-Light-Driven Photocatalytic Overall Water Splitting. ChemSusChem 11, 1365–1373.

Yapp C.J. (2001) Rusty relics of Earth history: Iron (III) oxides, isotopes, and surficial environments. Annual Review of Earth and Planetary Sciences. 29, 165–199.

Young G.M. (1976) Iron-formation and glaciogenic rocks of the Rapitan Group, Northwest Territories, Canada. Precambrian Res. 3, 137–158.

This is the peer-reviewed, final accepted version for American Mineralogist, published by the Mineralogical Society of America.
The published version is subject to change. Cite as Authors (Year) Title. American Mineralogist, in press.
DOI: https://doi.org/10.2138/am-2022-8843. http://www.minsocam.org/

778 **Table 1. Properties of Mn-substituted synthetic goethite samples.**

Mn	MCD (110)	MCD (020)	Unit cell dimension (nm)			IR reflection (cm^{-1})		
(mol %)	(nm)	(nm)	a (±1σ)	b (±1σ)	c (±1σ)	-OH	-OH	-OH
0	45.2	81	4.610 ± 0.002	9.953 ± 0.002	3.0189 ± 0.0007	3129	892	796
1.4	45.9	75.7	4.605 ± 0.001	9.955 ± 0.003	3.0182 ± 0.0005	3132	894	796
7.7	52.7	61.1	4.604 ± 0.001	9.982 ± 0.002	3.0150 ± 0.0005	3130	894	799
10.5	46.9	45.9	4.600 ± 0.001	9.988 ± 0.002	3.0130 ± 0.0006	3132	896	798
24.6	63.6	50.3	4.596 ± 0.002	10.026 ± 0.003	3.0087 ± 0.0009	3140	896	806

779 [1]MCD - mean crystallite diameter as estimated from XRD data.

780 **Table 2. Properties of Mn-substituted synthetic hematite samples.**

Mn	MCD (110)	MCD (104)	MCD(104)/ MCD(110)	Unit cell dimension (nm)		IR reflection (cm^{-1})		
(mol %)	(nm)	(nm)		a (±1σ)	c (±1σ)	Fe-O	Fe-O	unknown
0	82.5	18.8	0.22	5.003 ± 0.001	13.667 ± 0.004	434	520	1056
1.4	75	25.4	0.33	5.005 ± 0.002	13.680± 0.005	433	520	1055
7.7	56.9	21.7	0.38	5.011 ± 0.002	13.710 ± 0.006	435	521	1054
15.3	55.8	13.9	0.24	5.028 ± 0.004	13.781 ± 0.010	436	521	1051
28.5	35.4	12.6	0.33	5.030 ± 0.003	13.860 ± 0.009	439	521	1058

781 [1]MCD - mean crystallite diameter as estimated from XRD data.

782

This is the peer-reviewed, final accepted version for American Mineralogist, published by the Mineralogical Society of America.
The published version is subject to change. Cite as Authors (Year) Title. American Mineralogist, in press.
DOI: https://doi.org/10.2138/am-2022-8843. http://www.minsocam.org/

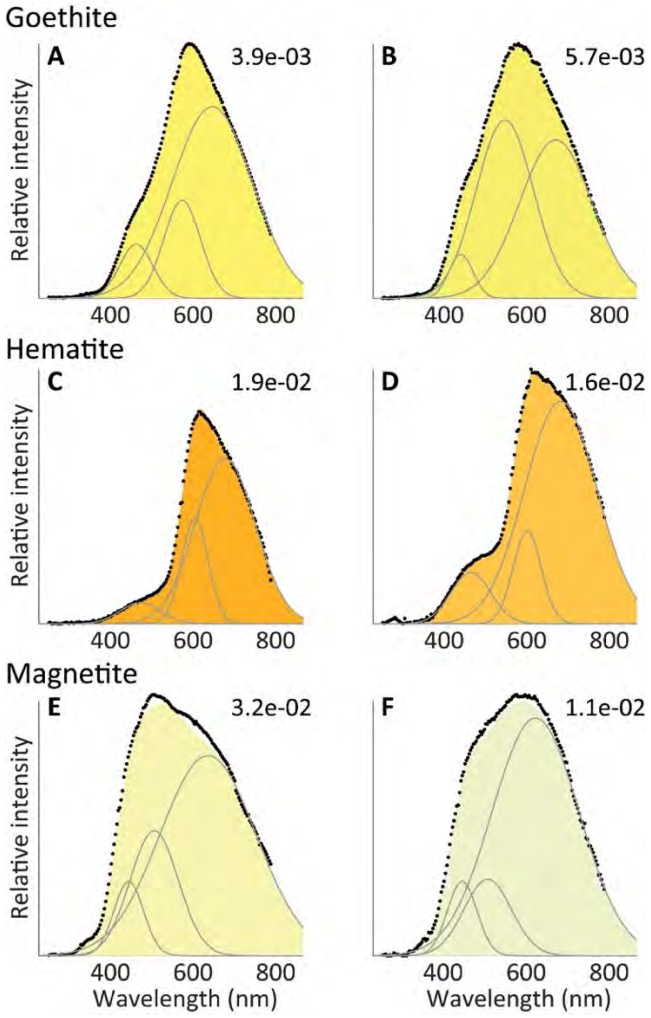

Figure 1. Examples of SEM-CL spectra of natural and synthetic Fe oxides and hydroxides. (A) SynG2, (B) NatG3, (C) SynH1, (D) NatH2, (E) SynM1 and (F) SynM2. The color of emitted light is shown as the infilled area under the spectra. Spectral deconvolution into Gaussian-shaped emission bands is shown in gray lines, and the sum of squared errors (SSE) between the fit and measurements is shown in the upper right of each panel.

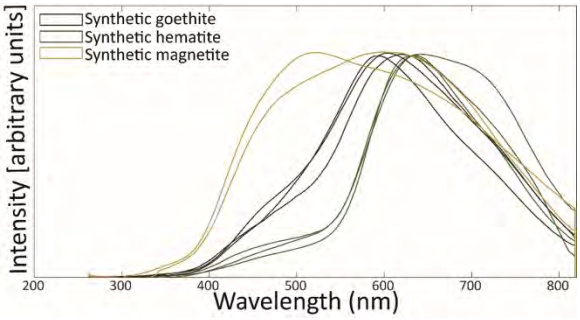

Figure 2. SEM-CL spectra of synthetic hematite, goethite and magnetite in this study.

This is the peer-reviewed, final accepted version for American Mineralogist, published by the Mineralogical Society of America.
The published version is subject to change. Cite as Authors (Year) Title. American Mineralogist, in press.
DOI: https://doi.org/10.2138/am-2022-8843. http://www.minsocam.org/

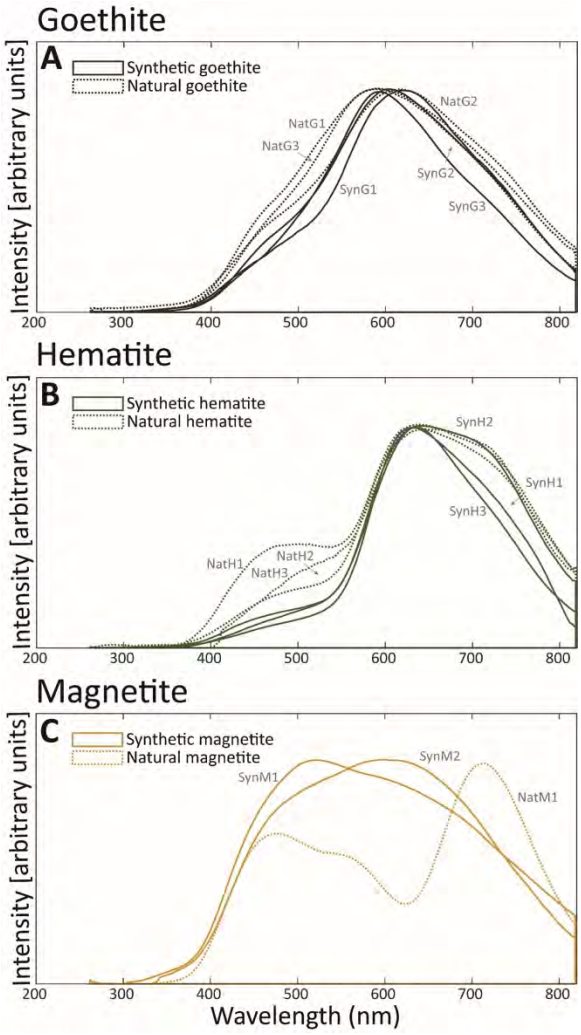

Figure 3. SEM-CL spectra of synthetic and natural (A) goethite, (B) hematite and (C) magnetite. Spectra of synthetic and natural samples are shown in solid and dotted lines, respectively. The sample names are shown as text on the figure panels.

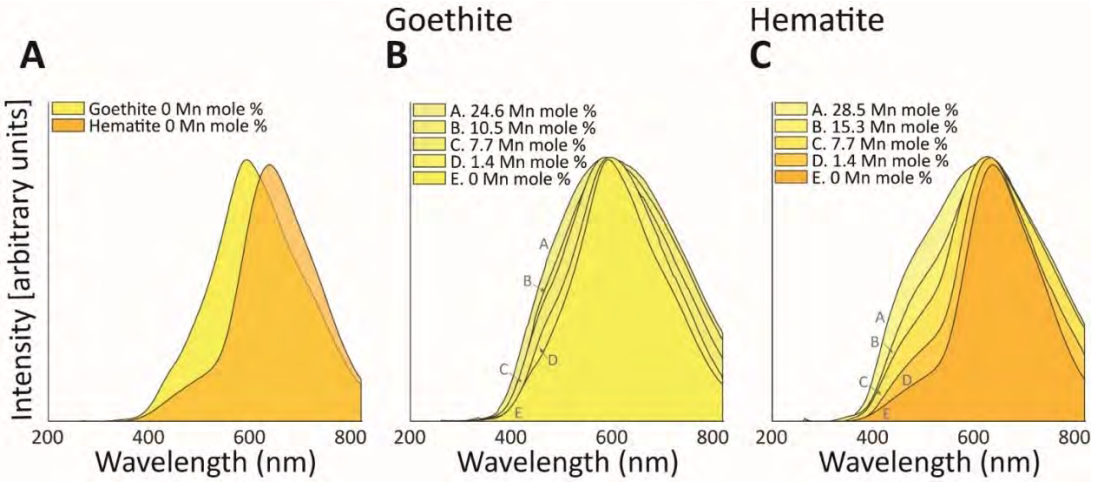

This is the peer-reviewed, final accepted version for American Mineralogist, published by the Mineralogical Society of America.
The published version is subject to change. Cite as Authors (Year) Title. American Mineralogist, in press.
DOI: https://doi.org/10.2138/am-2022-8843. http://www.minsocam.org/

797 **Figure 4.** SEM-CL spectra of Mn-substituted goethite and hematite. (A) Comparison of Mn-free
798 goethite and hematite spectra. (B) Goethite spectrum with increasing Mn substitution for Fe. (C)
799 Hematite spectrum with increasing Mn substitution for Fe. The color under individual spectra
800 represents their true color of emission.

801

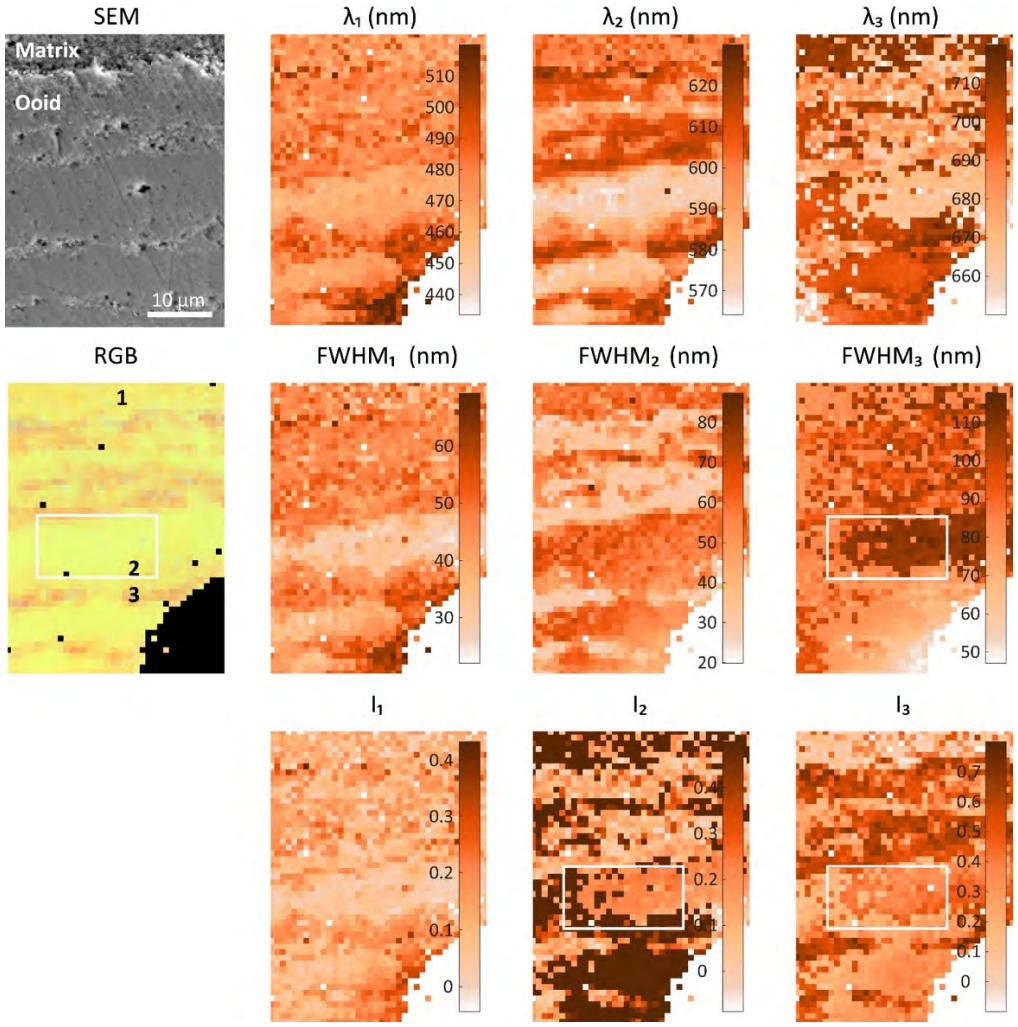

802

803 **Figure 5.** SEM image and SEM-CL maps of a goethite ooid from the Agbaja Formation
804 (App01). The SEM image shows the location of the ooid boundary, and the RGB image shows
805 the true color of CL emission and the location of three micro-Raman analyses, which confirmed
806 the existence of hematite. The maps of the spectral deconvolution parameters ($\lambda_{1\text{-}3}$, $FWHM_{1\text{-}3}$, $I_{1\text{-}3}$) show clear differences between the goethite and hematite, the latter of which was undetectable
807 by XRD. The maps further show differences within the goethite (e.g., $FWHM_3$, I_3), which are not
808 observable in the SEM image or in the emission color map (in white rectangle).
809

810

This is the peer-reviewed, final accepted version for American Mineralogist, published by the Mineralogical Society of America.
The published version is subject to change. Cite as Authors (Year) Title. American Mineralogist, in press.
DOI: https://doi.org/10.2138/am-2022-8843. http://www.minsocam.org/

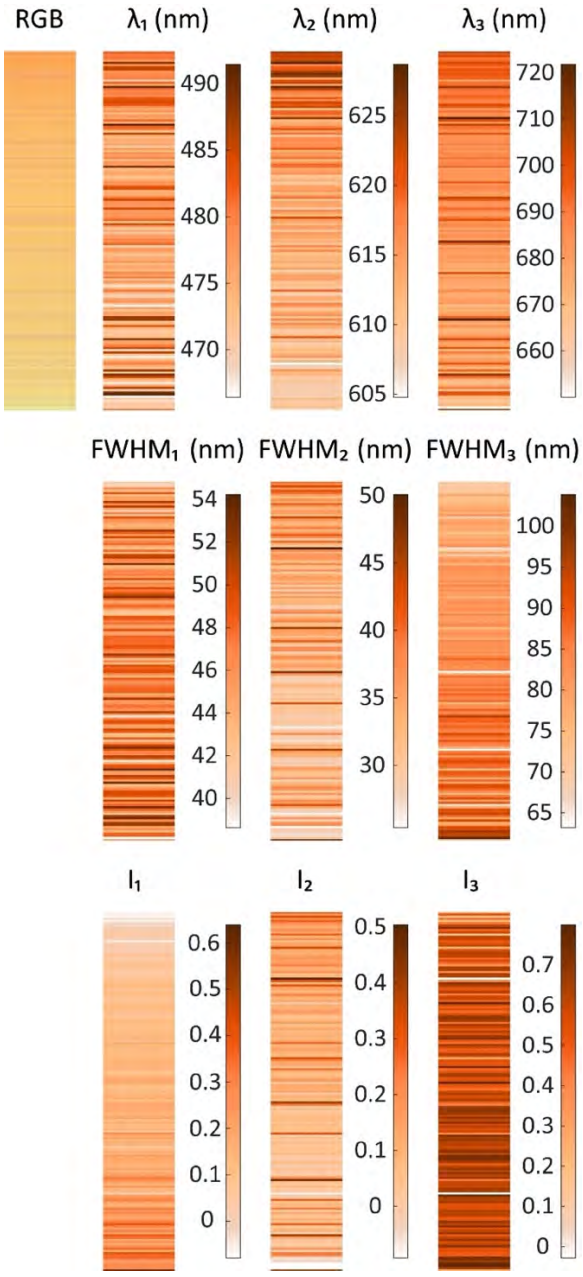

Figure 6. SEM-CL color and spectral parameters of point analyses of hematite in the Rapitan iron formation (App02).

This is the peer-reviewed, final accepted version for American Mineralogist, published by the Mineralogical Society of America.
The published version is subject to change. Cite as Authors (Year) Title. American Mineralogist, in press.
DOI: https://doi.org/10.2138/am-2022-8843. http://www.minsocam.org/

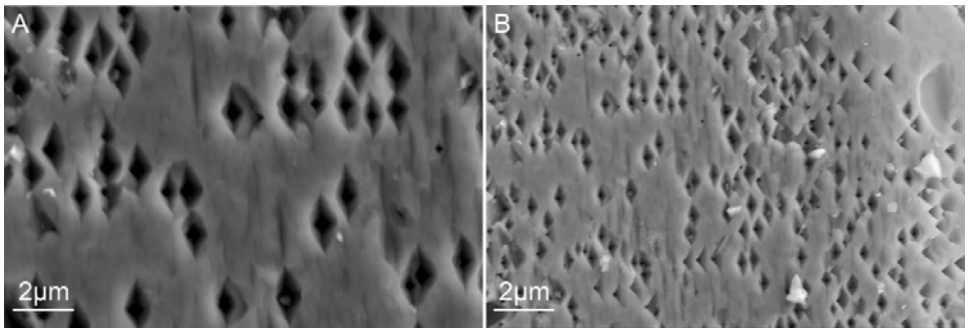

Figure 7. SEM images of natural magnetite 1 (NatM1), showing a high density of etch pits, which may be the source of the intense emission band at ≈725 nm.